J. Fluid Mech. (2006), *vol.* 551, *pp.* 93–116.
doi:10.1017/S0022112005008281 Printed in the United Kingdom

Resonant three-dimensional nonlinear sloshing in a square-base basin. Part 3. Base ratio perturbations

By ODD M. FALTINSEN, OLAV F. ROGNEBAKKE AND ALEXANDER N. TIMOKHA

Centre for Ships and Ocean Structures, NTNU, N-7491 Trondheim, Norway

(Received 15 December 2004 and in revised form 10 August 2005)

Previous parts studied nonlinear resonant sloshing in a prismatic tank under the academic assumption of a square base. However, a representative industrial tank may have an 'almost' rather than a 'precisely' square base. The present paper generalizes the multimodal technique of Part 1 to examine this complication. The main focus is on resonant sloshing due to lateral harmonic excitations, but several known theoretical results about free-standing waves have also been re-derived. The analysis shows that, although disturbances of the square base do not lead to new types of steady-state wave regimes, the frequency domains, where these wave regimes are stable, change considerably even with small perturbations of the breadth/width ratio around 1. The modifications of the effective frequency domains are compared with the results of two experimental series.

1. Introduction

The precursor of this paper (Part 1, Faltinsen, Rognebakke & Timokha 2003) developed an asymptotic modal method and derived a nonlinear modal system for modelling three-dimensional resonant sloshing in a square-base basin with finite depth. An inviscid and incompressible fluid with irrotational flow was assumed. The sloshing occurs because of horizontal harmonic excitation close to the lowest natural frequency. The main combined theoretical-and-experimental result of Part 1 is that a square cross-section causes the existence of three and only three physically different steady-state resonant regimes, i.e. 'planar', 'swirling' (rotary) and 'diagonal'-like ('squares'-like in Part 1). The excitation frequency ranges (effective frequency domains), where each steady-state regime is stable, are functions of the excitation amplitude and the fluid depth. Simultaneous instability of these regimes in a certain frequency range causes irregular, 'chaotic' waves.

The asymptotic modal technique of Part 1 assumed the smallness of the scaled excitation amplitude $\epsilon \ll 1$ (excitation amplitude/tank breadth ratio) and adopted the Moiseyev ordering (Moiseyev 1958; Faltinsen 1974), which matches the dominating modes with $O(\epsilon^{1/3})$. Error in prediction of the effective frequency domains is then of $o(\epsilon^{2/3})$ (intermediate and shallow depths require a special asymptotic technique and imply other accuracy, see, Faltinsen & Timokha 2002). The method required modifications (and accounting for damping) for accurate approximation of transient waves, in general, and transitions to steady-state wave regimes, in particular, for realistically small non-infinitesimal ϵ (Faltinsen, Rognebakke & Timokha 2005*a*, Part 2, reported corresponding results) and fails to describe local breaking phenomena at the

wall. However, as shown by Faltinsen, Rognebakke & Timokha (2005*b*), prediction of the effective frequency domains remains in very good agreement with experimental observations, especially for longitudinal forcing. Physically, this means that the nonlinear modal equations from Part 1 adequately capture the dominating, 'global' fluid flow involving the majority of the fluid mass, but amplification of higher modes due to transients and local wave breaking imply complex motions of smaller energy relative to this flow. Comparisons by Faltinsen *et al.* (2005*b*) demonstrated that, unless the excitation frequency approaches the bounds of the effective frequency domain, these relative motions may affect wave amplitudes, but not the types of motion. An additional particular explanation of the good agreement is that the dominating flow is formed by the two lowest natural modes (longest cross-waves) which are characterized by the lowest viscous damping rates. Owing to the well-known results of Keulegan (1959), general operator theory of linear viscous sloshing by Krein (1964) (see, also, reviews of these and related results by Krein & Langer 1978*a*, *b*; Kopachevsky & Krein 2003) and recent papers on asymptotic approximations by Martel, Nicolas & Vega (1998) and Miles & Henderson (1998), these rates are contributed by shear stress at the tank surface, of the order $O(\sqrt{\nu})$ (ν is non-dimensional kinematic viscosity) and, as shown by Faltinsen *et al.* (2005*b*), are less than ϵ in the experimental cases.

Bearing in mind the numerous industrial applications that can use the weakly nonlinear analysis on sloshing in mobile containers with a rectangular-shape base (an example is the liquefied natural gas tanks), the 'pure' square geometry is of limited relevance. The base ratio of realistic tanks may, in many cases, be close, but rarely equal to 1. This has been a predominating motivation for us to extend the results of Part 1, to resonant sloshing in tanks of nearly square cross-section, the more so, as the corresponding nonlinear asymptotic modal system should generally handle this complication. The focus was on identifying the types of steady-state wave regimes and quantifying their effective frequency domains. Numerical results on effective frequency domains were compared with observations during model tests from earlier experimental series (not published yet), which have been conducted in a basin with $60 \times 66\,\mathrm{cm}^2$ base. Besides, since the modal technique must be applicable to a study of nonlinear free-standing waves associated with the dominant character of the two lowest natural modes, another theoretical interest to the present paper consists of comparing it with the results of Bridges (1985, 1986, 1987). In particular, Bridges showed that perturbations of the base ratio yield a 'Poincaré'-type bifurcation of a 'planar' free-standing wave leading to a 'diagonal'-type sloshing. However, his technique did not detect 'swirling'-like free-standing waves established for an 'exactly' square base by Bryant & Stiassnie (1994, 1995). An evident query is whether 'swirling' disappears if the aspect ratio deviates from 1.

The three most important new theoretical results of the present paper are that:

(i) the nearly-square base causes the same three types of steady-state wave ('planar', 'swirling' (rotary) and nearly-'diagonal') for both free and longitudinally forced sloshing;

(ii) even small perturbations of the base ratio significantly change the frequency domain, where the steady-state resonant motions are stable; as a result, for non-small fluid depths, the range of 'chaotic' waves, which has been detected for sloshing in a square-base tank with finite depth, can be narrow or even disappear;

(iii) the free-standing 'swirling' waves do not disappear for perturbed base ratio. Similarly to the 'diagonal'-like type of free-standing waves established by Bridges (1987), occurrence of 'swirling' is associated with secondary bifurcations of the 'planar', Stokes waves.

In order to facilitate an independent reading of the paper without having earlier contributions available, we give in § 2 an introductory review of necessary formulations and results from Part 1, e.g. the non-dimensional free-boundary problem, physical and mathematical definitions as well as derivations associated with the modal modelling (Part 1, pp. 6–10). The analysis employs the nine-dimensional nonlinear asymptotic modal system (Part 1, p. 11) with forcing frequency close to the lowest natural frequency and is restricted to horizontal harmonic tank motions along a wall (lateral excitations). In § 3, we use the nonlinear modal system to re-derive several results by Bridges (1986) on secondary bifurcations of Stokes ('planar') free-standing waves in a nearly square-base basin. Along with the 'diagonal'-type of three-dimensional waves that have been detected in the Part 1, we find also a secondary bifurcation leading to 'swirling'.

In § 4, assuming small-amplitude longitudinal excitation, we establish the existence of the same three types of steady-state waves as for the square base. Examples are given of the behaviour of the corresponding response curves and their bifurcations. The main result of this section is that $O(\epsilon^{2/3})$-perturbations of the base ratio significantly affect the frequency domains, in which steady-state waves are realized. Theoretical predictions of the effective frequency domains are compared with experimental observations. One should note that the theoretical and experimental analysis of the resonant sloshing is restricted to non-small depths (the fluid depth-to-wall length ratios were larger than $h_1 = 0.3368\ldots$, where h_1 is the critical depth of the 'planar' sloshing, see, Waterhouse 1994; Faltinsen 1974; Faltinsen *et al.* 2003). Passage to smaller fluid depths can yield new phenomena, which require special systematic examinations (Ockendon, Ockendon & Waterhouse 1996; Ockendon & Ockendon 2001).

2. Preliminaries from Part 1

2.1. *Statement*

Let a rigid open rectangular base tank with breadth L_1 and width L_2 be partially filled by a perfect fluid with the mean depth h. We assume potential flow of an incompressible fluid and scale lengths by dividing by L_1, so that we consider a tank with breadth 1 and width $1/r = L_2/L_1$. Thus, values of the physical constants $h := h/L_1$, $g := g/L_1$ (g is the acceleration due to gravity) etc. are re-defined. This means that h in the following text is dimensionless and g has dimension $[\mathrm{s}^{-2}]$.

Furthermore, we fix the mobile coordinate system $Oxyz$ with the tank and superpose the Oxy-plane with the mean free surface so that the origin coincides with its centre and the Ox and Oy-axes are parallel to the vertical walls as shown in figure 1. The lateral harmonic excitations along the Ox-axis are described by the vector

$$\boldsymbol{v}_O(t) = (-\epsilon\sigma \sin\sigma t, 0, 0)^T \tag{2.1}$$

representing translatory velocity of the origin O relative to an absolute coordinate system. Here, σ is the forcing frequency and $\epsilon \ll 1$ is the scaled excitation amplitude.

The free-boundary problem on sloshing is based on a series of traditional physical idealizations implying inviscid potential flow and the absence of overturning waves and reads

$$\left.\begin{aligned} &\Delta\Phi = 0 \quad \text{in } Q(t);\ \frac{\partial\Phi}{\partial\nu} = \boldsymbol{v}_O\cdot\boldsymbol{\nu} \quad \text{on } S(t),\\ &\frac{\partial\Phi}{\partial\nu} = \boldsymbol{v}_O\cdot\boldsymbol{\nu} + \frac{f_t}{\sqrt{1+(\nabla f)^2}} \text{ on } \Sigma(t);\quad \int_{Q(t)} \mathrm{d}Q = \text{const},\\ &\frac{\partial\Phi}{\partial t} + \tfrac{1}{2}(\nabla\Phi)^2 - \nabla\Phi\cdot\boldsymbol{v}_O + gz = 0 \text{ on } \Sigma(t). \end{aligned}\right\} \tag{2.2}$$

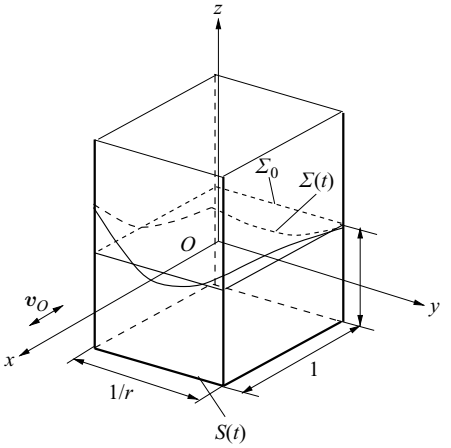

FIGURE 1. Sketch of a rectangular base tank oscillating along the Ox-axis. The fluid volume $Q(t)$ is confined to the free surface $\Sigma(t)$ and the wetted walls/bottom $S(t)$, its hydrostatic (mean) shape is determines by the planar unperturbed surface Σ_0.

Here the unknowns are the function $f(x, y, t)$ defining the free-surface evolution $\Sigma(t) : z = f(x, y, t) = 0$ and the absolute velocity potential $\Phi(x, y, z, t)$ which should be calculated in time-varying volume $Q(t)$ confined to the wetted body surface $S(t)$ and $\Sigma(t)$; $\boldsymbol{\nu}$ is outward normal to $Q(t)$.

The evolutional free-boundary problem should be completed by either initial or periodicity conditions. The initial (Cauchy) conditions require

$$f(x, y, t_0) = f_0(x, y); \quad \frac{\partial \Phi}{\partial \nu}\Big|_{\Sigma(t_0)} = \Phi_0(x, y, z) \tag{2.3}$$

to be known at $t = t_0$. Solutions of (2.2), (2.3) correspond to transient waves. The periodicity condition

$$f(x, y, t + T) = f(x, y, t); \quad \nabla\Phi(x, y, z, t + T) = \nabla\Phi(x, y, z, t) \tag{2.4}$$

($T = 2\pi/\sigma$ is the forcing period) implies the steady-state wave motions.

2.2. *Modal representation*

When $\boldsymbol{v}_O = \mathbf{0}$, the linearized (2.2) has fundamental solutions that describe natural waves $\Phi = \exp(\mathrm{i}\sigma_{i,j}t)\varphi_{i,j}(x, y, z)$, ($\mathrm{i}^2 = -1$), where

$$\varphi_{i,j}(x, y, z) = f_i^{(1)} f_j^{(2)} \frac{\cosh(\lambda_{i,j}(z + h))}{\cosh(\lambda_{i,j}h)},$$
$$\lambda_{i,j} = \pi\sqrt{i^2 + r^2 j^2}, \quad \sigma_{i,j}^2 = g\lambda_{i,j}\tanh(\lambda_{i,j}h), \quad i, j \geqslant 0, \quad i + j \neq 0, \tag{2.5}$$

$\sigma_{i,j}$ are the natural frequencies and $\varphi_{i,j}$ are the natural modes.

Projections of $\varphi_{i,j}$ on the mean free surface $z = 0$ introduce the shapes of linear standing waves $f_{i,j}(x, y) = f_i^{(1)}(x) f_j^{(2)}(y) = \varphi_{i,j}|_{z=0}$. Physically, $f_{i,j}$ can be classified in terms of two subclasses. The first consists of two-dimensional Stokes wave shapes in the Oxz- and Oyz-planes. Corresponding natural modes have often been called 'planar' waves. These are

$$f_i^{(1)}(x) = \cos(\pi i(x + 1/2)), \quad i \geqslant 1; \quad f_j^{(2)}(y) = \cos(\pi j r(y + 1/(2r))), \quad j \geqslant 1. \tag{2.6}$$

The other subclass defines three-dimensional wave patterns

$$f_i^{(1)}(x) \cdot f_j^{(2)}(y), \quad i, j \geqslant 1. \tag{2.7}$$

Sometimes, the analysis must be extended to introduce the mixed (called 'diagonal'- or 'squares'-like) modes

$$C_1 f_i^{(1)}(x) - C_2 f_i^{(2)}(y), \quad C_1 C_2 \neq 0, \tag{2.8}$$

recombining two Stokes modes of (2.6) into three-dimensional 'diagonal' patterns with non-zero weight coefficients C_1 and C_2.

The set $\{f_{i,j}(x, y),\ i+j \geqslant 1\}$ represents an appropriate Fourier basis in the horizontal rectangular cross-section of the tank $[-1/2, 1/2] \times [-1/(2r), 1/(2r)]$; $\{\varphi_{i,j}(x, y, z),\ i + j \geqslant 1\}$ is a complete system of harmonic functions in the unperturbed fluid domain $Q_0 = [-1/2, 1/2] \times [-1/(2r), 1/(2r)] \times [-h, 0]$, which satisfies zero-Neumann boundary conditions on the tank surface. Following the general modal scheme by Faltinsen *et al.* (2000) (see, the original equations (3.4), (3.6) and (3.7)), Part 1 introduces the modal representation of the free-surface elevation $z = f(x, y, t)$ as

$$f(x, y, t) = \sum_{i+j \geqslant 1}^{\infty} \beta_{i,j}(t) f_{i,j}(x, y), \tag{2.9}$$

where $\beta_{i,j}$ are the generalized coordinates governing the evolution of each i, j-mode.

2.3. *Asymptotic nonlinear modal system*

If the width/breadth aspect ratio $r = L_1/L_2$ is equal to 1, the natural spectrum $\{\sigma_{i,j},\ i + j \geqslant 1\}$ has an infinite set of double eigenvalues $\sigma_{i,j} = \sigma_{j,i},\ i \neq j$ generating strong inter-resonances between the modes $f_{i,j}$ and $f_{j,i}$ and, as a consequence, a high multiplicity of steady-state (periodic) solutions related to both free-standing waves (Bridges 1987; Bryant & Stiassnie 1994, 1995) and resonant waves (Part 1). Passage to $r \approx 1$ implies splitting the natural frequencies $\sigma_{i,j},\ i \neq j$.

Following the procedure in Part 1, we evaluate the primary resonance $\sigma \to \sigma_{1,0} \sim \sigma_{0,1}$ and introduce the so-called Narimanov–Moiseyev modal ordering (Moiseyev 1958; Narimanov 1957; Miles 1984, 1994; Feng & Sethna 1989, and others) of the generalized coordinates $\beta_{i,j},\ i + j \geqslant 1$ (modal functions) as follows

$$\beta_{1,0} \sim \beta_{0,1} = O(\epsilon^{1/3}); \quad \beta_{2,0} \sim \beta_{1,1} \sim \beta_{0,2} = O(\epsilon^{2/3}); \quad \beta_{i,j} \leqslant O(\epsilon), \quad i + j \geqslant 3. \tag{2.10}$$

It holds true as $\epsilon \to 0$, $h = O(1)$ and captures the primary resonant phenomena with two dominating modes $f_{1,0}$ and $f_{0,1}$. The Narimanov–Moiseyev ordering is consistent with the third-order analysis by Bridges (1987) and Bryant & Stiassnie (1995) for free nonlinear sloshing regimes associated with amplification of the lowest natural modes.

Tedious derivations of Part 1 established that, if (2.10) is fulfilled, asymptotic approximation of f up to $O(\epsilon)$ requires only nine modal functions $\beta_{i,j}(t),\ i + j \leqslant 3$ in the Fourier series (2.9). The modal functions are solutions of a system of nonlinear ordinary differential equations (modal system, Part 1, p. 11). After re-denoting for brevity

$$\beta_{1,0} = a_1; \quad \beta_{2,0} = a_2; \quad \beta_{0,1} = b_1; \quad \beta_{0,2} = b_2; \quad \beta_{1,1} = c_1,$$
$$\beta_{3,0} = a_3; \quad \beta_{2,1} = c_{21}; \quad \beta_{1,2} = c_{12}; \quad \beta_{0,3} = b_3 \tag{2.11}$$

and taking into account (2.1), we can re-write the nonlinear modal system in the form

$$\begin{aligned}
&\left[\ddot{a}_1+\sigma_{1,0}^2a_1+d_1(\ddot{a}_1a_2+\dot{a}_1\dot{a}_2)+d_2\left(\ddot{a}_1a_1^2+\dot{a}_1^2a_1\right)+d_3\ddot{a}_2a_1-P_{1,0}^{(1)}\epsilon\sigma^2\cos\sigma t\right]\\
&\quad+d_6\ddot{a}_1b_1^2+\ddot{b}_1(d_7c_1+d_8a_1b_1)+d_9\ddot{c}_1b_1+d_{10}\dot{b}_1^2a_1+d_{11}\dot{a}_1\dot{b}_1b_1+d_{12}\dot{b}_1\dot{c}_1=0, \qquad (2.12a)\\
&\left[\ddot{b}_1+\sigma_{0,1}^2b_1+\bar{d}_1(\ddot{b}_1b_2+\dot{b}_1\dot{b}_2)+\bar{d}_2\left(\ddot{b}_1b_1^2+\dot{b}_1^2b_1\right)+\bar{d}_3\ddot{b}_2b_1\right]+\bar{d}_6\ddot{b}_1a_1^2\\
&\quad+\ddot{a}_1(\bar{d}_7c_1+\bar{d}_8a_1b_1)+\bar{d}_9\ddot{c}_1a_1+\bar{d}_{10}\dot{a}_1^2b_1+\bar{d}_{11}\dot{a}_1\dot{b}_1a_1+\bar{d}_{12}\dot{a}_1\dot{c}_1=0, \qquad (2.12b)\\
&\left[\ddot{a}_2+\sigma_{2,0}^2a_2+d_4\ddot{a}_1a_1+d_5\dot{a}_1^2\right]=0, \qquad (2.12c)\\
&\left[\ddot{b}_2+\sigma_{0,2}^2b_2+\bar{d}_4\ddot{b}_1b_1+\bar{d}_5\dot{b}_1^2\right]=0, \qquad (2.12d)\\
&\ddot{c}_1+\hat{d}_1\ddot{a}_1b_1+\hat{d}_2\ddot{b}_1a_1+\hat{d}_3\dot{a}_1\dot{b}_1+\sigma_{1,1}^2c_1=0, \qquad (2.12e)
\end{aligned}$$

$$\left[\ddot{a}_3+\sigma_{3,0}^2a_3+\ddot{a}_1\left(q_1a_2+q_2a_1^2\right)+q_3\ddot{a}_2a_1+q_4\dot{a}_1^2a_1+q_5\dot{a}_1\dot{a}_2-P_{3,0}^{(1)}\epsilon\sigma^2\cos\sigma t\right]=0, \qquad (2.13a)$$

$$\begin{aligned}
&\ddot{c}_{21}+\sigma_{2,1}^2c_{21}+\ddot{a}_1(q_6c_1+q_7a_1b_1)+\ddot{b}_1\left(q_8a_2+q_9a_1^2\right)+q_{10}\ddot{a}_2b_1+q_{11}\ddot{c}_1a_1\\
&\qquad+q_{12}\dot{a}_1^2b_1+q_{13}\dot{a}_1\dot{b}_1a_1+q_{14}\dot{a}_1\dot{c}_1+q_{15}\dot{a}_2\dot{b}_1=0, \qquad (2.13b)\\
&\ddot{c}_{12}+\sigma_{1,2}^2c_{12}+\ddot{b}_1(\bar{q}_6c_1+\bar{q}_7a_1b_1)+\ddot{a}_1\left(\bar{q}_8b_2+\bar{q}_9b_1^2\right)+\bar{q}_{10}\ddot{b}_2a_1+\bar{q}_{11}\ddot{c}_1b_1\\
&\qquad+\bar{q}_{12}\dot{b}_1^2a_1+\bar{q}_{13}\dot{a}_1\dot{b}_1b_1+\bar{q}_{14}\dot{b}_1\dot{c}_1+\bar{q}_{15}\dot{a}_1\dot{b}_2=0, \qquad (2.13c)\\
&\left[\ddot{b}_3+\sigma_{0,3}^2b_3+\ddot{b}_1\left(\bar{q}_1b_2+\bar{q}_2b_1^2\right)+\bar{q}_3\ddot{b}_2b_1+\bar{q}_4\dot{b}_1^2b_1+\bar{q}_5\dot{b}_1\dot{b}_2\right]=0, \qquad (2.13d)
\end{aligned}$$

where

$$\begin{aligned}
&P_{i,j}^{(1)}=\frac{2\delta_{0j}E_{i,0}}{(\pi i)^2}[(-1)^i-1], \quad P_{i,j}^{(2)}=\frac{2\delta_{0i}E_{0,j}}{r(\pi j)^2}[(-1)^j-1],\\
&E_{i,j}=\lambda_{i,j}\tanh(\lambda_{i,j}h), \quad \lambda_{i,j}=\pi\sqrt{i^2+r^2j^2}
\end{aligned} \qquad (2.14)$$

and coefficients $d_1, \bar{d}_i, \hat{d}_i, q_i$ and $\bar{q}_i$ are functions of depth (see explicit computational formulae in Part 1).

2.4. *Steady-state asymptotic solutions for harmonic forcing*

In the asymptotic limit $\epsilon\to 0$, the modal system (2.12) can be asymptotically integrated for periodic solutions by combining the Bubnov–Galerkin method with asymptotic expansions. The third-order solutions (up to $O(\epsilon)$) are given in Part 1 ((3.8)–(3.9)). The lowest-order quantities of these solutions are determined by four real numbers (amplitudes) $A, \bar{A}, \bar{B}$ and $B=O(\epsilon^{1/3})$ appearing for a_1 and b_1, i.e.

$$a_1(t)=A\cos(\sigma t)+\bar{A}\sin(\sigma t)+o\left(\epsilon^{1/3}\right);\ b_1(t)=\bar{B}\cos(\sigma t)+B\sin(\sigma t)+o\left(\epsilon^{1/3}\right). \qquad (2.15)$$

The remaining asymptotic contribution is of $o(\epsilon^{1/3})$. The dominating amplitudes should be found from the following system of algebraic equations (see, Part 1, (3.10))

$$\left.\begin{aligned}
&A(\Gamma_{1,0}+m_1(A^2+\bar{A}^2)+m_2\bar{B}^2+m_3B^2)+(m_2-m_3)\bar{A}\bar{B}B-P_1=0,\\
&\bar{A}(\Gamma_{1,0}+m_1(A^2+\bar{A}^2)+m_2B^2+m_3\bar{B}^2)+(m_2-m_3)AB\bar{B}=0,\\
&\bar{B}(\Gamma_{0,1}+\bar{m}_1(B^2+\bar{B}^2)+\bar{m}_2A^2+\bar{m}_3\bar{A}^2)+(\bar{m}_2-\bar{m}_3)\bar{A}AB=0,\\
&B(\Gamma_{0,1}+\bar{m}_1(B^2+\bar{B}^2)+\bar{m}_2\bar{A}^2+\bar{m}_3A^2)+(\bar{m}_2-\bar{m}_3)\bar{A}A\bar{B}=0,
\end{aligned}\right\} \qquad (2.16)$$

where

$$\left.\begin{aligned}
&\Gamma_{i,j} = \bar{\sigma}_{i,j}^2 - 1, \quad \bar{\sigma}_{i,j} = \frac{\sigma_{i,j}}{\sigma}; \quad P_1 = P_{1,0}^{(1)}\epsilon,\\
&m_1 = -\tfrac{1}{2}d_2 - d_1\left(p_0 - \tfrac{1}{2}r_0\right) - 2r_0 d_3;\\
&m_2 = -\tfrac{3}{4}d_6 + \tfrac{1}{4}d_{10} - \tfrac{3}{4}d_8 + \tfrac{1}{4}d_{11} - d_7 p_1 - r_1\left(\tfrac{1}{2}d_7 + 2d_9 - d_{12}\right),\\
&m_3 = -\tfrac{1}{4}d_6 + \tfrac{3}{4}d_{10} - \tfrac{1}{4}d_8 - \tfrac{1}{4}d_{11} - r_1\left(\tfrac{1}{2}d_7 + 2d_9 - d_{12}\right),\\
&p_0 = \frac{d_4 - d_5}{2\bar{\sigma}_{2,0}^2}; \quad r_0 = \frac{d_4 + d_5}{2\left(\bar{\sigma}_{2,0}^2 - 4\right)},\\
&p_1 = \frac{\hat{d}_1 + \hat{d}_2 - \hat{d}_3}{2\bar{\sigma}_{1,1}^2}; \quad r_1 = \frac{\hat{d}_1 + \hat{d}_2 + \hat{d}_3}{2\left(\bar{\sigma}_{1,1}^2 - 4\right)}
\end{aligned}\right\} \tag{2.17}$$

and $\bar{m}_i,\ i = 1, 2, 3$ are obtained from (2.17) by adding bars over the coefficients of the modal system d_i. The coefficients $m_i, \bar{m}_i$ are functions of the non-dimensional depth h, the forcing frequency σ and r.

Depending on the values m_i and $\bar{m}_i$, the system (2.16) does not always have real solutions and may have multiple solutions. Part 1 presented a detailed mathematical analysis and derived the resolvability conditions, but its conclusions are only valid for $r = 1$. The next section will generalize them to the nearly-square case ($0 < |r-1| \ll 1$) for free-standing waves ($P_1 = 0$) and longitudinal forcing ($P_1 \neq 0$).

3. Free nonlinear standing waves

3.1. *Three types of free-standing wave*

The dominating contribution into third-order asymptotic solutions, which describe the nonlinear free-standing waves, are formed by the lowest modes (1, 0) and (0, 1)

$$f(x, y, t) = (A\cos\sigma t + \bar{A}\sin\sigma t) f_1^{(1)}(x) + (\bar{B}\cos\sigma t + B\sin\sigma t) f_1^{(2)}(y) + o\left(\epsilon^{1/3}\right), \tag{3.1}$$

where $A, \bar{A}, B$ and $\bar{B}$ are computed from the system (2.16) with $P_1 = 0$. In this case, the system (2.16) is homogeneous and, therefore, includes the trivial solution $A = \bar{A} = B = \bar{B} = 0$.

Since any unforced solution of conservative mechanical systems is invariant relative to phase shift $t =: t + t_0$ and, without loss of generality, we assume that

$$\bar{A} = 0$$

in (3.1). The latter leads to the necessary resolvability condition of (2.16)

$$(m_2 - m_3) A B \bar{B} = 0, \tag{3.2}$$

and taking into account the numerical results of Part 1 (see also some details in the next paragraph) establishing that $m_2 \neq m_3$, we find three and only three physically different types of nonlinear free-standing wave associated with non-trivial solutions of (2.16).

(i) Stokes, 'planar' waves along either the Ox-axis for

$$A \neq 0; \quad B = \bar{B} = 0,$$

or the Oy-axis with

$$A = 0; \quad B^2 + \bar{B}^2 \neq 0.$$

Both non-trivial solutions above are associated with the primary bifurcations of the trivial solution at the points $\sigma = \sigma_{1,0}$ and $\sigma = \sigma_{0,1}$, respectively.

The first solution, which implies non-zero A, can be treated as points on the branch

$$\gamma_{1,0}: \quad \Gamma_{1,0} + m_1 A^2 = 0, \tag{3.3}$$

in the $(\sigma/\sigma_{1,0}, |A|)$-plane.

The second case requires an introduction of the resulting amplitude $b = \sqrt{B^2 + \bar{B}^2}$ and determines the branch

$$\gamma_{0,1}: \quad \Gamma_{0,1} + \bar{m}_1 b^2 = 0 \tag{3.4}$$

in the $(\sigma/\sigma_{1,0}, b)$-plane (generally, owing to phase-shift invariance, we may also assume $B = 0$ and operate only with $\bar{B}$).

(ii) 'Square'-like or, throughout this paper, 'diagonal' waves are associated with the nonlinear solutions

$$A \neq 0, \quad \bar{B} \neq 0, \quad B = 0,$$

which lead to standing-wave patterns by the mixed mode (2.8)

$$f(x, y, t) = \left(A f_1^{(1)}(x) + \bar{B} f_1^{(2)}(y)\right) \cos \sigma t + o\left(\epsilon^{1/3}\right).$$

In that case, the system (2.16) transforms to the form

$$m_1 A^2 + m_2 \bar{B}^2 = -\Gamma_{1,0}, \quad \bar{m}_1 \bar{B}^2 + \bar{m}_2 A^2 = -\Gamma_{0,1},$$

which is a system of linear equations with respect to A^2 and $\bar{B}^2$. If $m_1 \bar{m}_1 - m_2 \bar{m}_2 \neq 0$, the system has a unique solution which, accounting for the positiveness of A^2 and B^2, can be re-written in the form

$$A^2 = \frac{\Gamma_{0,1} m_2 - \Gamma_{1,0} \bar{m}_1}{m_1 \bar{m}_1 - m_2 \bar{m}_2} > 0; \quad \bar{B}^2 = \frac{\Gamma_{1,0} \bar{m}_2 - \Gamma_{0,1} m_1}{m_1 \bar{m}_1 - m_2 \bar{m}_2} > 0. \tag{3.5}$$

The first conclusion about 'diagonal' waves is that they are associated with a triad $(\sigma/\sigma_{1,0}, A \neq 0, \bar{B} \neq 0)$ and, therefore, determine a three-dimensional response curve. Besides, if $r \neq 1$, then $\Gamma_{1,0}$ and $\Gamma_{0,1}$ on the right-hand side of (3.1) cannot be equal to zero, simultaneously, and, therefore, solutions (3.5) differ from zero and $\sqrt{A^2 + \bar{B}^2} \neq 0$ along the response curves. Since the response curves do not intersect the horizontal axis, the 'diagonal' wave cannot appear owing to a primary bifurcation of the trivial solution, but rather as a secondary bifurcation of the 'planar' solution.

(iii) 'Swirling' waves

$$f(x, y, t) = A f_1^{(1)}(x) \cos \sigma t + B f_1^{(2)}(y) \sin \sigma t + o\left(\epsilon^{1/3}\right)$$

are associated with solutions conditions

$$A \neq 0, \quad \bar{B} = 0, \quad B \neq 0.$$

Repeating the analytical manipulations of (ii), these can be found as a triad $(\sigma/\sigma_{1,0}, A \neq 0, B \neq 0)$ determined by

$$A^2 = \frac{\Gamma_{0,1} m_3 - \Gamma_{1,0} \bar{m}_1}{m_1 \bar{m}_1 - m_3 \bar{m}_3} > 0; \quad B^2 = \frac{\Gamma_{1,0} \bar{m}_3 - \Gamma_{0,1} m_1}{m_1 \bar{m}_1 - m_3 \bar{m}_3} > 0. \tag{3.6}$$

If $r \neq 1$, these solutions can appear only because of a secondary bifurcation, following the same argumentation as for 'diagonal' case.

3.2. *Asymptotic analysis of* (i)–(iii)

The dependence of the dominating amplitudes on $\sigma/\sigma_{1,0}$ (governed by (3.3)–(3.6)) can be examined by a direct computation. However, the presence of small parameters

associated with the closeness of $\sigma_{1,0}$ and $\sigma_{0,1}$ makes it possible to implement an asymptotic technique, which is mathematically equivalent to Bridges (1985, 1987) for the splitting frequencies $\sigma_{1,0}$ and $\sigma_{0,1}$ as $r \neq 0$ (in the finite-depth case $h = O(1)$).

3.2.1. *Matching asymptotics*

Consider r close to 1 so that

$$r = 1 + \mu, \quad \frac{1}{r} = 1 - \mu + o(\mu), \tag{3.7}$$

$\sigma \to \sigma_{1,0}$ and let ϵ be the third-order (highest) contribution in the asymptotic approximation of a free-standing wave.

In order to express μ and $\sigma/\sigma_{1,0} \approx \sigma/\sigma_{0,1}$ in a scale of ϵ, we should match the lowest-order terms in (2.16). Because the dominating amplitudes A, B and $\bar{B}$ are of $O(\epsilon^{1/3})$, simple analysis shows that

$$\Gamma_{1,0} \sim \Gamma_{0,1} = O\left(\epsilon^{2/3}\right) \tag{3.8}$$

and, therefore,

$$\sigma = \sigma_{1,0} + O\left(\epsilon^{2/3}\right) = \sigma_{0,1} + O\left(\epsilon^{2/3}\right). \tag{3.9}$$

Further,

$$\frac{\sigma_{1,0}^2}{\sigma^2} = \frac{\sigma_{1,0}^2}{\sigma^2} - \mu\sigma_0 + o(\mu); \quad \sigma_0 = 1 + \frac{2\pi h}{\sinh(2\pi h)}, \tag{3.10}$$

and, as a consequence,

$$\mu = O\left(\epsilon^{2/3}\right). \tag{3.11}$$

The relationships (3.7), (3.9) and (3.11) make it possible to deduce

$$m_i(h, \sigma, r) = m_i^0(h) + O\left(\epsilon^{2/3}\right); \quad \bar{m}_i(h, \sigma, r) = m_i^0(h) + O\left(\epsilon^{2/3}\right), m_i^0 = m_i(h, \sigma_{1,0}, 0). \tag{3.12}$$

Neglecting the terms $o(\epsilon)$ in (2.16) and accounting for $\bar{A} = 0$ leads to the following system with respect to A, B and $\bar{B}$

$$\left.\begin{aligned} &A\left(\Gamma_{1,0} + m_1^0 A^2 + m_2^0 \bar{B}^2 + m_3^0 B^2\right) = 0, \\ &\bar{B}\left(\Gamma_{1,0} + \mu\sigma_0 + m_1^0(B^2 + \bar{B}^2) + m_2^0 A^2\right) = 0, \\ &B\left(\Gamma_{1,0} + \mu\sigma_0 + m_1^0(B^2 + \bar{B}^2) + m_3^0 A^2\right) = 0, \end{aligned}\right\} \tag{3.13}$$

where the coefficients m_i^0 are functions of the depth h.

3.2.2. *Free-standing waves versus h*

Since the sign of $\mu = L_1/L_2 - 1$ depends on the position of the Oxy-plane, i.e. placing Ox along the longer walls always gives $\mu > 0$, the consideration of the free-standing waves is for brevity restricted to $\mu > 0$. Besides, the case $\mu < 0$ will follow from these considerations by rotating the Oxy-plane around the Oz-axis and performing appropriate substitutions between A and $\bar{B}$, $\bar{A}$ and B.

'Planar' waves. Owing to (3.3) and (3.4), the branches (the so-called 'backbones') $\gamma_{1,0}$, $i + j = 1$ emerging owing to primary bifurcation of the trivial solution are asymptotically governed by

$$\gamma_{1,0}: \quad \Gamma_{1,0} + m_1^0 A^2 = 0 \tag{3.14}$$

for 'planar' waves along the Ox-axis. Analogously,

$$\gamma_{0,1}: \quad \Gamma_{1,0} + \mu\sigma_0 + m_1^0 b^2 = 0 \tag{3.15}$$

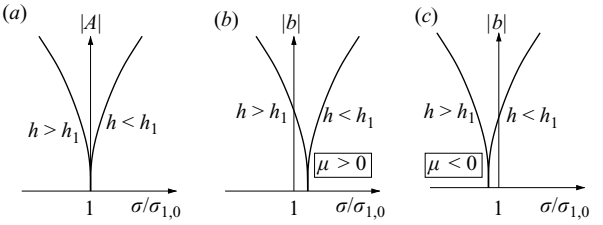

FIGURE 2. The primary bifurcations associated with (*a*) 'planar' longitudinal and (*b, c*) cross-waves.

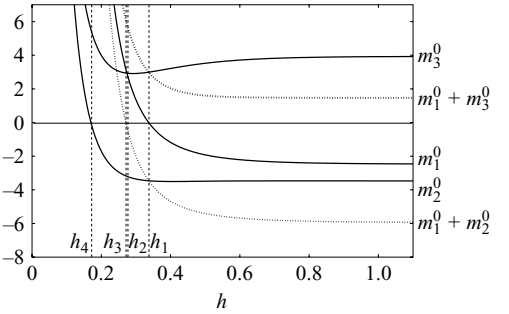

FIGURE 3. The graphs representing $m_i^0(h)$, $i = 1, 2, 3$ and some of their linear combinations versus depth/breadth ratio h. The root of $m_1^0(h) = 0$ gives $h_1 = 0.3477\ldots$, the depth $h_2 = 0.274\ldots$ implies the equality $m_1^0 = m_3^0$, $h_3 = 0.27\ldots$ is computed from $m_1^0 + m_2^0 = 0$ and $h_4 = 0.17\ldots$ for $m_2^0 = 0$.

describes cross-waves, i.e. 'planar' waves along the Oy-axis, appearing owing to the primary bifurcation at $\sigma_{0,1}$.

'Soft'- or 'hard-spring' behaviour of the backbones $\gamma_{1,0}$ and $\gamma_{0,1}$ depends on the sign of m_1^0, which becomes zero at $h_1 = 0.3368\ldots$ (see discussion of this critical depth by Waterhouse 1994; Faltinsen *et al.* 2003, and figure 3). The local branching at the primary bifurcation of the trivial solution is schematically depicted in figure 2. It shows that the non-zero μ causes a shift of $\gamma_{0,1}$.

In contrast to 'planar' waves, evaluation of 'diagonal' and 'swirling' introduces a larger set of critical depths h_i associated with zeros of both m_i^0 and their linear combinations. Following Faltinsen *et al.* (2003) we facilitate this analysis by the graphs in figure 3, which detect h_1 at $m_1^0 = 0$ and $h_2 = 0.274\ldots$, $(m_1^0 = m_3^0)$, $h_3 = 0.27\ldots$, $(m_1^0 + m_2^0 = 0)$, $h_4 = 0.17\ldots$, $(m_2^0 = 0)$.

'Diagonal' waves. The asymptotic solutions of (3.5) can be found from

$$\gamma_1 : \ \Gamma_{1,0} - \mu\frac{\sigma_0 m_2^0}{m_1^0 - m_2^0} + \left(m_1^0 + m_2^0\right)A^2 = 0,$$

$$\gamma_2 : \ \Gamma_{1,0} + \mu\frac{\sigma_0 m_1^0}{m_1^0 - m_2^0} + \left(m_1^0 + m_2^0\right)\bar{B}^2 = 0,$$

where γ_1 and γ_2 determine the longitudinal, along the Ox-axis, and transversal amplitude components of the 'diagonal' waves and can be considered as projections of the triad $(\sigma/\sigma_{1,0}, |A|, |\bar{B}|)$ on the $(\sigma/\sigma_{1,0}, |A|)$ and $(\sigma/\sigma_{1,0}, |\bar{B}|)$-planes, respectively. Parts (*a*) and (*b*) of figures 4–7 show γ_1 and γ_2 for different depths and $\mu > 0$.

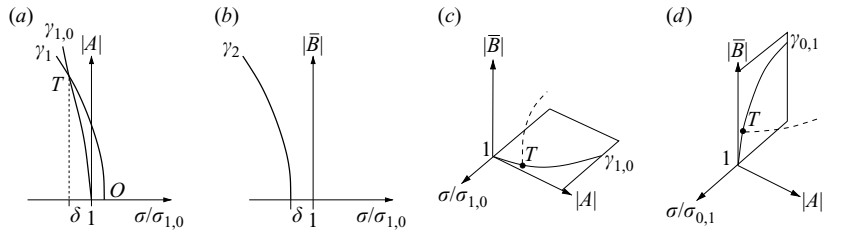

FIGURE 4. The secondary bifurcation (the point T) associated with appearance of 'diagonal' from 'planar' waves; the case of the fluid depths $h > h_1$. The 'planar' waves are associated with points on the planar curves $\gamma_{1,0}$ and $\gamma_{0,1}$, while the 'diagonal' regimes correspond to three-dimensional curves in the $(\sigma/\sigma_{1,0}, |A|, |\bar{B}|)$-coordinate system. (*a*) and (*b*) show the $(\sigma/\sigma_{1,0}, |A|)$ and $(\sigma/\sigma_{1,0}, |\bar{B}|)$-projections of the branching for $\mu > 0$, so that the curves γ_1 and γ_2 are defined in § 3.2.2. The resolvability condition $\bar{B}^2 > 0$ determines the range $\sigma/\sigma_{1,0} < \delta$, where the 'diagonal' regime exists, and, therefore, the arc OT does not imply 'diagonal' waves. (*c*) shows the three-dimensional branching for $\mu > 0$ and (*d*) is related to $\mu < 0$. Here, the 'planar' waves correspond to points on the solid lines, while the three-dimensional 'diagonal' waves are posed as points on the dashed lines.

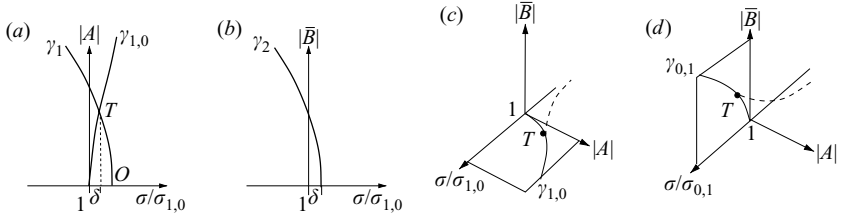

FIGURE 5. The same as in figure 4, but for $h_3 < h < h_1$.

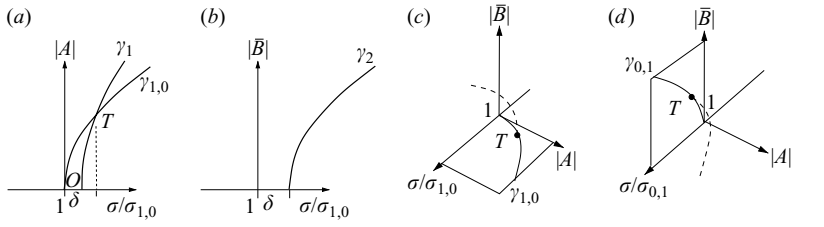

FIGURE 6. The same as in figure 4, but for $h_4 < h < h_3$.

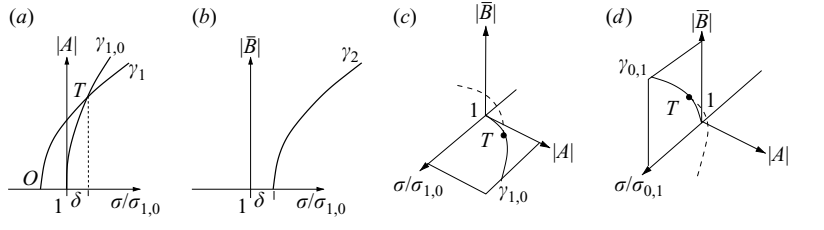

FIGURE 7. The same as in figure 4, but for $h < h_4$.

The 'diagonal' regimes exist only if both $A^2 > 0$ and $\bar{B}^2 > 0$. If either A or $\bar{B}$ become equal to zero, the 'diagonal' regime switches to the 'planar' solutions (i) and therefore, intersections of γ_1 with $\gamma_{1,0}$ or γ_2 with $\gamma_{0,1}$ define the secondary (Poincaré-type)

bifurcation. Considering $h \neq h_3$ implies $m_2^0 \neq 0$ and, therefore, appearance of the intersections depends on μ, which determines the non-zero shift of $\gamma_i,\ i = 1, 2$, relative to the origin at $\sigma/\sigma_{1,0} = 1$. If $\mu = 0$ (square tank), γ_1 coincides with γ_2, both curves emerge from the origin $\sigma/\sigma_{1,0} = 1$ and, since $\gamma_{1,0}$ and $\gamma_{0,1}$ also bifurcate from the origin, the intersection disappears. If $\mu \neq 0$, the shift between γ_1 and $\gamma_{1,0}$ as well as between γ_2 and $\gamma_{0,1}$ is unavoidable and the intersection at a point T becomes possible. The analysis detects the presence of T for all non-critical depths as it is shown in Part (a) of figures 4–7.

The secondary bifurcation at T (for the dual natural modes $f_{i,j}$ and $f_{j,i},\ i \neq j$), which is associated with intersections of the 'planar' and 'diagonal' response branches was first predicted by Bridges (1985, 1987). He used direct expansions of the original free-boundary problem and exemplified the behaviour of the branches for the pair of modes (1, 2), (2, 1) and various depths based on finite and shallow-water asymptotics. Being motivated by the behaviours of the pair (1, 0), (0, 1) we give below an additional representation of both the local branching and appearance of T for different non-dimensional depths h away from three critical values h_1, h_3 and h_4, where the 'diagonal' wave response changes its 'soft' or 'hard-spring' behaviour and/or position relative to the primary resonance at $\sigma/\sigma_{1,0} = 1$. The results are treated in the $(\sigma/\sigma_{1,0}, |A|)$ and $(\sigma/\sigma_{1,0}, |\bar{B}|)$-planes in parts ($a$) and ($b$) of figures 4–7 and in the three-dimensional view $(\sigma/\sigma_{1,0}, |A|, |\bar{B}|)$ in part (c) of figures 4–7. Part (d) of figures 4–7 show also three-dimensional interpretation of the secondary bifurcations for $\mu < 0$. The analysis of the primary bifurcation of the trivial solution as well as the secondary bifurcation (the local branching in a neighbourhood of T) is easily based on relationships between $m_i^0,\ i = 1, 2, 3$. The larger fluid depths (the case $h > h_1$) give, for instance, $m_1^0 < 0, m_2^0 < 0, m_1^0 + m_2^0 < 0, m_1^0 - m_2^0 > 0$ and formal solutions of (3.16) determine the 'soft-spring' curves in figure 4 (a, b). The curves γ_1 and γ_2 change their 'soft-spring' behaviour with h. This is demonstrated in figure 5 (a, b) ($h_3 < h < h_1,\ m_1^0 > 0, m_2^0 < 0, m_1^0 + m_2^0 < 0, |m_1^0| < |m_2^0|$), figure 6 ($a, b$) ($h_4 < h < h_3,\ m_1^0 > 0, m_2^0 < 0, m_1^0 + m_2^0 > 0, |m_1^0| > |m_2^0|$) and figure 7 ($a$–$d$) ($h < h_4,\ m_1^0 > 0, m_2^0 > 0, m_1^0 + m_2^0 > 0$). An important fact is that the appearance of 'diagonal' waves occurs from 'planar' waves along the longest length of the tank, namely, from $\gamma_{1,0}$ as $r > 1$ and from $\gamma_{0,1}$ as $r < 1$.

The investigations of the local branching at T involve the resolvability condition $A^2 > 0,\ \bar{B}^2 > 0$, which should be fulfilled on γ_1 and γ_2. The non-zero shift between γ_1 and γ_2 makes this condition not satisfied along both curves. For $\mu > 0$, simple analysis shows that the abscissa of the origin of γ_2 coincides with the abscissa of T and points on the arc OT do not imply the 'diagonal' regime, because there are no appropriate real $\bar{B}$ in the corresponding frequency range on the $\sigma/\sigma_{1,0}$-axis. The bifurcation at T consists therefore of three curves as shown in parts (c) and (d) of figures 4–7.

'Swirling' waves. The asymptotic solutions associated with 'swirling' are defined by

$$\gamma_3 : \Gamma_{1,0} - \mu \frac{\sigma_0 m_3^0}{m_1^0 - m_3^0} + \left(m_1^0 + m_3^0\right) A^2 = 0,$$

$$\gamma_4 : \Gamma_{1,0} + \mu \frac{\sigma_0 m_1^0}{m_1^0 - m_3^0} + \left(m_1^0 + m_3^0\right) B^2 = 0.$$

Again, as in the case of 'diagonal' regimes, if $\mu = 0$, the branches γ_3 and γ_4 coincide and their intersection with $\gamma_{1,0}$ and $\gamma_{0,1}$, respectively, is not possible. For non-zero μ, the local branches γ_3 and γ_4 are shifted both relative to each other and relative to

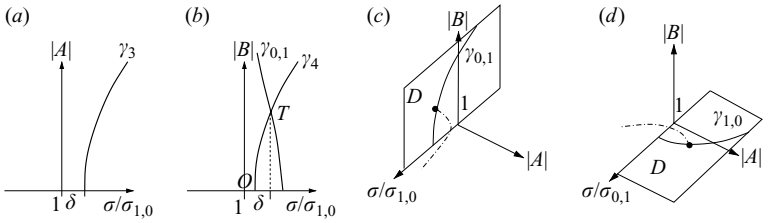

FIGURE 8. The secondary bifurcation (the point D) associated with the appearance of 'swirling' from 'planar' waves; the case of the fluid depths $h > h_1$. The 'planar' waves are associated with points on the planar curves $\gamma_{1,0}$ and $\gamma_{0,1}$, while the 'swirling' regimes correspond to three-dimensional curves in the $(\sigma/\sigma_{1,0}, |A|, |B|)$-coordinate system. (*a*) and (*b*) show the $(\sigma/\sigma_{1,0}, |A|)$ and $(\sigma/\sigma_{1,0}, |B|)$-projections of the branching for $\mu > 0$, so that the curves γ_3 and γ_4 are defined in § 3.2.2. The resolvability condition $B^2 > 0$ determines the range $\sigma/\sigma_{1,0} > \delta$, where the 'swirling' regime exists, and, therefore, the arc OD does not imply 'swirling' waves. (*c*) shows the three-dimensional branching for $\mu > 0$ and (*d*) is related to $\mu < 0$. Here, the 'planar' wave correspond to points on the solid lines, while the three-dimensional 'swirling' waves are posed as points on the dash-and-dot lines.

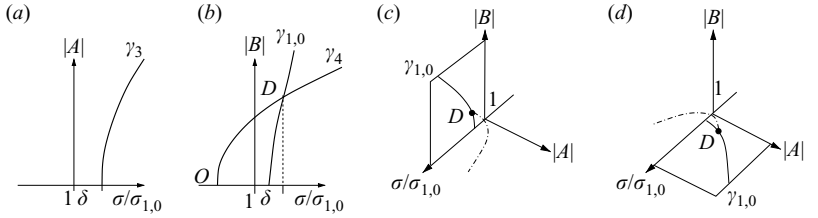

FIGURE 9. The same as in figure 8, but for $h_2 < h < h_1$.

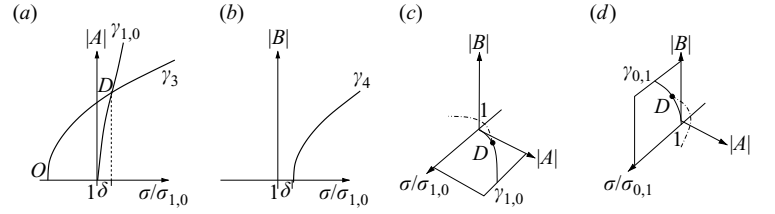

FIGURE 10. The same as in figure 8, but for $h < h_2$.

$\gamma_{i,j},\ i+j=1$. Their intersections with one from $\gamma_{i,j},\ i+j=1$ determine the secondary bifurcation (the point D) of the corresponding 'planar' wave and the appearance of the 'swirling' regime. The analysis of the secondary bifurcation is similar to the case of the 'diagonal' regimes. Corresponding drawings are in figures 8–10. Here, figure 8 corresponds to $h > h_1$ $(m_1^0 < 0, m_3^0 > 0, m_1^0 + m_3^0 > 0, |m_3^0| > |m_1^0|)$, figure 9 implies $h_2 < h < h_1,\ m_1^0 > 0, m_3^0 > 0, m_1^0 + m_3^0 > 0, m_3^0 > m_1^0$ and figure 10 is related to $h < h_2, m_1^0 > 0, m_3^0 > 0, m_1^0 + m_3^0 > 0, m_1^0 > m_1^0$.

In contrast to 'diagonal' waves, non-small depths $h > h_2$ cause the appearance of 'swirling' regimes at D from 'planar' waves along the shorter side. In order to demonstrate this point, we represent the joint bifurcation pictures in figure 11.

4. Resonant steady-state waves

Repeating analytical manipulations of Part 1 for $P_1 \neq 0$ (p. 17) we can obtain the following resolvability condition of (2.17): $A \neq 0, \bar{A} = 0$ and $B\bar{B} = 0$. An exhaustive

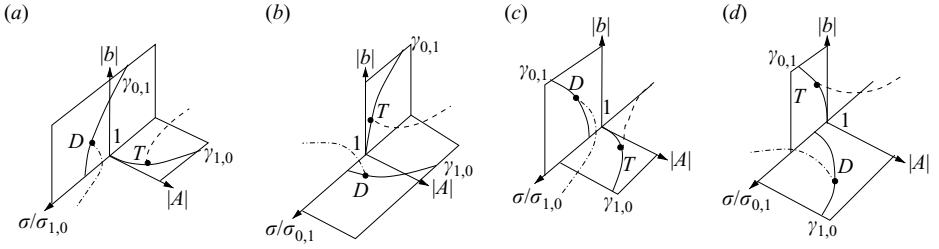

FIGURE 11. The secondary bifurcations associated with appearance of 'diagonal' from 'planar' longitudinal waves (the point T) and 'swirling' from 'planar' transversal waves (the point D). 'Planar' waves are constituted by points on the solid line, 'diagonal' by the dashed line and 'swirling' by the dash-and-dot line. (*a*) $\mu > 0,\ h > h_1$; (*b*) $\mu < 0,\ h > h_1$; (*c*) $\mu > 0,\ h_2 < h < h_1$; (*d*) $\mu < 0,\ h_2 < h < h_1$.

search for appropriate variants gives exactly the same types of steady-state regime as for a 'pure' square base, namely, (i) 'planar' waves in the forcing plane ($A \neq 0, \bar{A} = 0, B = \bar{B} = 0$), (ii) 'diagonal' (or 'squares'-like) waves ($A \neq 0, \bar{A} = 0, \bar{B} \neq 0, B = 0$) and (iii) 'swirling' waves ($A \neq 0, \bar{A} = 0, \bar{B} = 0, B \neq 0$). In contrast to free-standing waves, the Stokes wave along the Oy-axis is not realized.

The three steady-state regimes (i)–(iii) may be stable or unstable depending on the depth h, the base ratio r and the actual forcing amplitude ϵ.

4.1. *Asymptotic analysis*

4.1.1. *Governing equations*

Simple analysis shows that the matching asymptotics $\mu \sim \epsilon^{2/3}$ of the previous paragraph is allowable for the forced case $0 < \epsilon \to 0$. Besides, repeating the derivation from this paragraph, we arrive at the governing asymptotic equations for steady-state regimes:

$$A\left(\Gamma_{1,0} - m_1^0 A^2\right) = P_1 \tag{4.1}$$

for 'planar' longitudinal waves;

$$A\left(\Gamma_{1,0} + m_1^0 A^2 m_2^0 \bar{B}^2\right) = P_1; \quad \Gamma_{1,0} + \mu\sigma_0 + m_1^0 \bar{B}^2 m_2^0 A^2 = 0$$

for 'diagonal' waves, which can be re-expressed as

$$A\left[\Gamma_{1,0} - \mu\frac{\sigma_0 m_2^0}{m_1^0 - m_2^0} + \left(m_1^0 + m_2^0\right)A^2\right] = \frac{m_1^0 P_1}{m_1^0 - m_2^0}; \quad \bar{B}^2 = -\frac{1}{m_1^0}\left[\Gamma_{1,0} + \mu\sigma_0 + m_2^0 A^2\right] > 0 \tag{4.2}$$

and, finally, 'swirling' waves are governed by

$$A\left[\Gamma_{1,0} - \mu\frac{\sigma_0 m_3^0}{m_1^0 - m_3^0} + \left(m_1^0 + m_3^0\right)A^2\right] = \frac{m_1^0 P_1}{m_1^0 - m_3^0}; \quad B^2 = -\frac{1}{m_1^0}\left[\Gamma_{1,0} + \mu\sigma_0 + m_3^0 A^2\right] > 0. \tag{4.3}$$

The equations (4.1)–(4.3) show that three-dimensional solutions (ii) and (iii) have no joint solutions in the $(\sigma/\sigma_{1,0}, A, \bar{B}, B)$-space, but each three-dimensional solution can theoretically have joint points with (4.1). These points are associated with intersections in the $(\sigma/\sigma_{1,0}, A)$ of the branches (4.1) and branches $\gamma_5 :\ \Gamma_{1,0} + \mu\sigma_0 + m_2^0 A^2 = 0$ and $\gamma_6 :\ \Gamma_{1,0} + \mu\sigma_0 + m_3^0 A^2 = 0$, respectively.

4.1.2. *Stability and the types of bifurcation*

Assuming that only perturbations of the dominating order $\epsilon^{1/3}$ are important and following the scheme of Part 1, we introduce the slowly varying time $\tau = \epsilon^{2/3}\sigma t/2$,

the Moiseyev asymptotics $\Gamma_{1,0} \sim \Gamma_{0,1} \sim \mu \sim O(\epsilon^{2/3})$ and express the infinitesimally perturbed dominant solutions as

$$\begin{aligned} a_1 &= (A + \alpha(\tau))\cos\sigma t + (\bar{A} + \bar{\alpha}(\tau))\sin\sigma t + o\big(\epsilon^{1/3}\big), \\ b_1 &= (\bar{B} + \bar{\beta}(\tau))\cos\sigma t + (B + \beta(\tau))\sin\sigma t + o\big(\epsilon^{1/3}\big), \end{aligned} \tag{4.4}$$

where A, $\bar{A}$, B and $\bar{B}$ are the solutions of (2.16) and $\alpha, \bar{\alpha}, \beta$ and $\bar{\beta}$ are their relative perturbations depending on τ. Inserting (4.4) into (2.12)–(2.13), gathering terms of the lowest asymptotic order and keeping linear terms in $\alpha, \bar{\alpha}, \beta$ and $\bar{\beta}$ lead to the following linear system of ordinary differential equations

$$\boldsymbol{c}' + \mathbf{C}\boldsymbol{c} = 0, \tag{4.5}$$

where $\boldsymbol{c} = (\alpha, \bar{\alpha}, \beta, \bar{\beta})^T$ and the matrix $\mathbf{C}$ has the following elements

$$\begin{aligned}
&c_{11} = -[2A\bar{A}m_1 + (m_2 - m_3)B\bar{B}],\ c_{12} = -[\bar{\sigma}_1^2 - 1 + m_1A^2 + 3m_1\bar{A}^2 + m_2B^2 + m_3\bar{B}^2], \\
&c_{13} = -[2\bar{A}Bm_2 + (m_2 - m_3)A\bar{B}],\ c_{14} = -[2\bar{A}\bar{B}m_3 + (m_2 - m_3)AB], \\
&c_{21} = \bar{\sigma}_1^2 - 1 + 3m_1A^2 + m_1\bar{A}^2 + m_2\bar{B}^2 + m_3B^2,\ c_{22} = 2A\bar{A}m_1 + (m_2 - m_3)B\bar{B}, \\
&c_{23} = 2ABm_3 + (m_2 - m_3)\bar{A}\bar{B},\ c_{24} = 2A\bar{B}m_2 + (m_2 - m_3)\bar{A}B, \\
&c_{31} = 2m_2A\bar{B} + (m_2 - m_3)B\bar{A},\ c_{32} = 2m_3\bar{A}\bar{B} + (m_2 - m_3)AB, \\
&c_{33} = 2m_1B\bar{B} + (m_2 - m_3)A\bar{A},\ c_{34} = \bar{\sigma}_1^2 - 1 + m_1B^2 + 3m_1\bar{B}^2 + m_2A^2 + m_3\bar{A}^2, \\
&c_{41} = -[2m_3AB + (m_2 - m_3)\bar{A}\bar{B}],\ c_{42} = -[2\bar{A}Bm_2 + (m_2 - m_3)A\bar{B}], \\
&c_{43} = -[\bar{\sigma}_1^2 - 1 + 3m_1B^2 + m_1\bar{B}^2 + m_2\bar{A}^2 + m_3A^2],\ c_{44} = -[2B\bar{B}m_1 + (m_2 - m_3)A\bar{A}].
\end{aligned}$$

Stability of the fixed point solutions A, $\bar{A}$, B and $\bar{B}$ depends on the eigenvalues of the matrix $\mathbf{C}$. Computations give the following characteristic polynomial

$$\lambda^4 + c_1\lambda^2 + c_0 = 0, \tag{4.6}$$

where c_0 is the determinant of $\mathbf{C}$ and c_1 is a complicated function of the elements of $\mathbf{C}$. The necessary and sufficient conditions for the real part of the roots of the quartic equation (4.6) to be non-positive – i.e. for the perturbations $\alpha, \bar{\alpha}, \beta$ and $\bar{\beta}$ be stable – are

$$c_0 > 0, \quad c_1 > 0, \quad c_1^2 - 4c_0 > 0. \tag{4.7}$$

Computing $c_i,\ i = 0, 1, 2$ may help to classify the types of the bifurcation points (see details by Miles 1984). A vanishing c_0 determines the turning point or the Poincaré bifurcation, but changing sign of the discriminant $c_1^2 - 4c_0$ indicate the so-called Hamiltonian Hopf-bifurcation points (furthermore, the Hopf bifurcation). Note that the position of the bifurcation points is defined to within $o(\epsilon^{2/3})$ and, therefore, if damping rates (estimated by Keulegan 1959; Krein 1964; Martel *et al.* 1998; Faltinsen *et al.* 2005*b*, as $O(\sqrt{\nu})$, where ν is the scaled viscosity), or other physical factors contribute in the proposed scheme $O(\epsilon^{2/3})$, this position may significantly change.

4.2. *Three-dimensional steady-state regimes*

For different depths h, resonant three-dimensional wave motion in basins of square cross-section has been investigated in Part 1. The effect of the non-dimensional exciting amplitude ϵ was analysed in Faltinsen *et al.* (2005*b*), where it is shown that, in contrast to h, ϵ does not change the qualitative character of bifurcations leading to the three-dimensional sloshing, but can increase/decrease the frequency domains in

which these steady-state motions are stable. This implies a 'sliding' of the bifurcation points with varying ϵ, but never their disappearance.

In the present paper, the base ratio r is a supplementary parameter to h and ϵ, which can strongly affect results on steady-state sloshing. Even though both h and ϵ are fixed, varying the parameter r around 1 plays a significant role in changing the character of bifurcations. We tested numerous relevant combinations of h, ϵ and r and, after analysing them, have found that dependencies of bifurcation phenomena on r are qualitatively the same for each of the ranges $h > h_1$, $h_2 < h < h_1$, $h_3 < h < h_2$, $h_4 < h < h_4$ and $h < h_4$. Taking into account the results by Faltinsen & Timokha (2002) on applicability of the asymptotic theories based on the Moiseyev relationships for resonant waves and the importance of higher modes with decreasing h, the consideration below concentrates on the case $h > h_1$.

4.2.1. *Bifurcations leading to 'diagonal' waves, branching*

When $r \leqslant 1$, the response curves representing the 'diagonal' motions versus $\sigma/\sigma_{1,0}$ are qualitatively similar to those found for square cross-section (Part 1). New types of branch accompanied by the Hopf- or Poincaré-type bifurcations are established only for $r > 1$. In order to illustrate this point, we give four examples in figures 12(*a*)–12(*d*) ordered with increasing r. Since the computations of the resonant longitudinal waves involve non-zero A, the three-dimensional curves in the $(\sigma/\sigma_{1,0}, |A|, |\bar{B}|)$-frame are accompanied by their projections on the $(\sigma/\sigma_{1,0}, |A|)$-plane. All the definitions related to the points F, W etc. are presented in the caption of figure 12.

Our stability analysis technique makes it possible to distinguish stable (solid lines), unstable (dashed lines) solutions as well as to detect both the turning- and Hopf-bifurcation points on the three-dimensional response curves. The starting case is in figure 12(*b*) (similar to figure 5(*b*) in Part 1, but with other denotation for bifurcation points) that corresponds to $r = 1$, where F is the Poincaré-bifurcation point yielding the 'diagonal' regime from the 'planar' response curve and V is the turning point. Decreasing r (figure 12*a*) indicates a left 'drift' of the response curves responsible for the 'diagonal' regimes so that the Poincaré-bifurcation point F replaces the turning point P (for the 'planar' branch). It becomes a separator between stable and unstable solutions.

Increasing r (excitation along the longer walls) changes the response curves dramatically. A positive, but still relatively small $\mu = r - 1$, develops a right shift of the 'diagonal' response curves along $\sigma/\sigma_{1,0}$-axis. As a result, the point F moves up, along the 'planar' response curve, but the $\bar{B}$-component around the point V decreases. If we continue increasing μ, the branch with V will have not one, but rather three bifurcation points (figure 12*c*) that are denoted as V_i, $i = 1, 2, 3$. Here, V_1 is the turning point, but two Hopf-bifurcation points V_2 and V_3 constitute a zone of instability between them. One interesting fact is that $r = 1.065$ in case (*c*) implies stable 'diagonal' waves (between V_2 and V_1) for a small zone around $\sigma/\sigma_{1,0} = 1$. Existence of such a zone was not possible for a square base with finite depth h.

A consequent increase of r decreases the $\bar{B}$-component between V_1 and V_2 and leads to the situation depicted in figure 12(*d*), where the response curve responsible for the 'diagonal' regime 'touches' the $(\sigma/\sigma_{1,0}, |A|)$-plane. The edge between V_1 and V_2 becomes responsible for the 'planar' response curve. The points V_1 and V_2 are then the Poincaré-bifurcations, but V_3 and V_4 imply the Hopf-bifurcations. A collateral effect of this regeneration of V_i, $i = 1, 2$ is the appearance of stable 'planar' waves in the vicinity of $\sigma/\sigma_{1,0} = 1$ that is impossible for a square base.

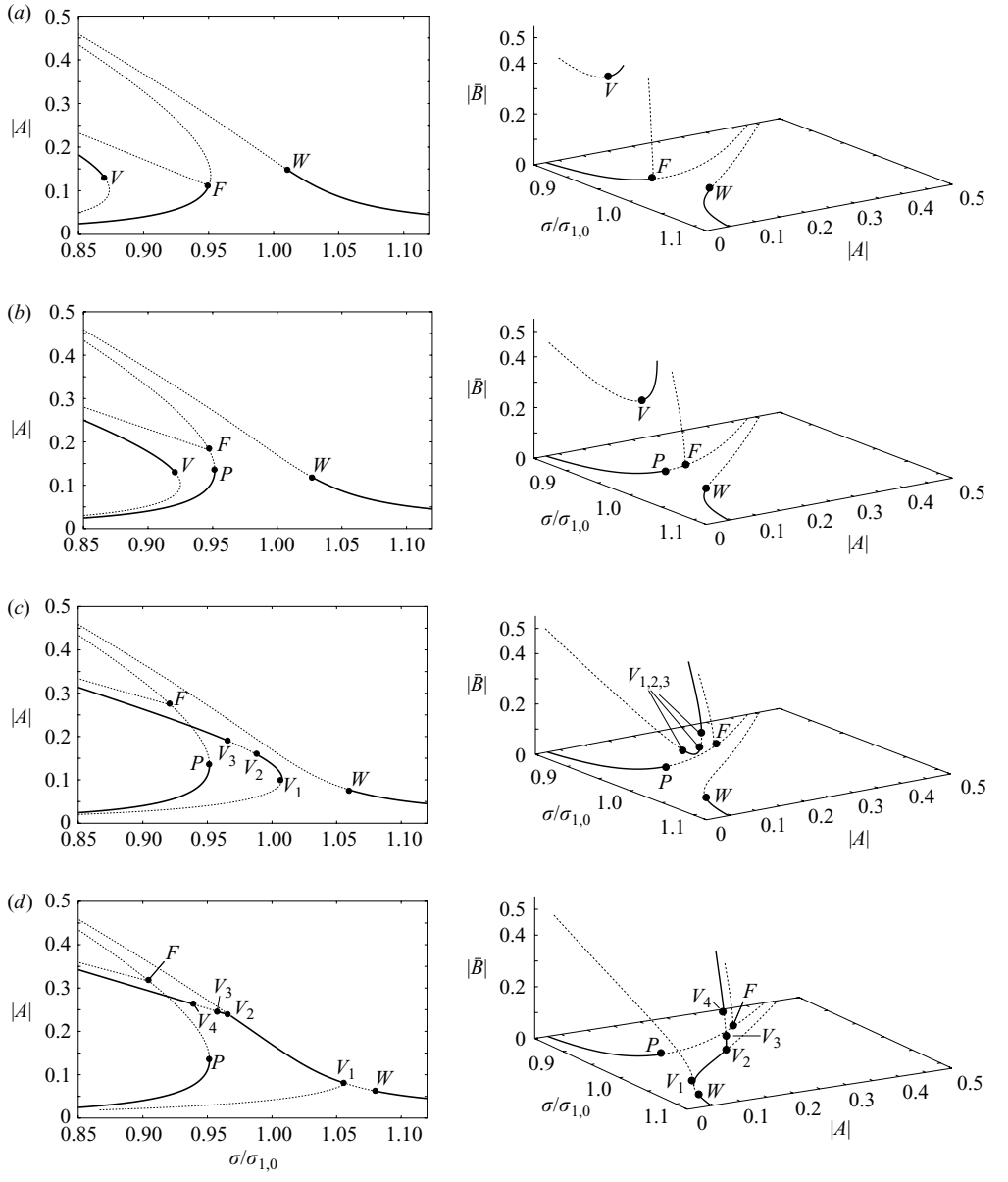

FIGURE 12. Resonance curves responsible for 'planar' and 'diagonal' waves versus r for finite depths ($h > h_1$). The calculations are made for $h = 0.5$ and $\epsilon = 0.008$ and this is related to our experiments. Four values of r are considered: (*a*) $r = 0.95$, (*b*) $r = 1$ (square cross-section), (*c*) $r = 1.065$ and (*d*) $r = 1.1$. The graphs represent dependence of $|A|$ on $\sigma/\sigma_{1,0}$ and the three-dimensional branching in the $(\sigma/\sigma_{1,0}, |A|, |\bar{B}|)$-coordinate system. The solid lines imply stable solutions and the dashed lines indicate instability of the corresponding branches. The point W is related to bifurcations leading to the 'swirling' regime (see details in figure 13), but other points are caused by the 'diagonal' regimes: F implies the bifurcation point yielding three-dimensional, 'diagonal' waves from the 'planar' regime, P corresponds to the turning point of the 'planar' response, the points $V(V_1)$, V_2, V_3 and V_4 evolve (with increasing r) from a single turning point V for the 'diagonal' motions to two Poincaré-bifurcation (V_1 and V_2) and two Hopf-bifurcation points (V_3 and V_4) in case (*d*).

4.2.2. *Bifurcations leading to 'swirling' waves, branching*

Three-dimensional response curves (in the $(\sigma/\sigma_{1,0}, |A|, |B|)$-coordinate system) and their projections (on the $(\sigma/\sigma_{1,0}, |A|)$-plane), which are responsible for the 'planar' and 'swirling' regimes, are shown in figure 13. Their evaluation starts from the case $r = 1$ shown in figure 13(c) (except for the names of the critical points, this case is equivalent to figure 5(c) from Part 1). Three-dimensional curves in figure 13(c) correspond to 'swirling'. They contain the Poincaré-bifurcation (point W) and the Hopf-bifurcation (point U).

In contrast to the 'diagonal' regimes, both increasing and decreasing r are able to change the qualitative features of the branching. Increasing r (figure 13a, b) moves the abscissa of U in the right and yields the turning point W_1 on the 'swirling' response curve (note that appearance of V_2 and V_3 is associated with 'diagonal' waves). When $r < 1$, W moves left along the corresponding 'planar' response curve, but the point U falls into the triplet of the Hopf-bifurcation points U_1, U_2 and U_3, so that the edge between U_1 and U_2 becomes responsible for stable 'swirling' periodic solutions (figure 13d). Further, the B-component on the response curve between U_1 and U_2 decreases with decreasing r and this stable zone transforms to the stable 'planar' regime bounded by two Poincaré-bifurcation points U_1 and U_2 as shown in figure 13(e).

An interesting physical conclusion following from figure 13(d, e) is that excitation along the shorter walls ($r < 1$) may both increase the zone of stable 'planar' wave due to drift of W close to $\sigma/\sigma_{1,0}$ and increase the probability of the stable 'swirling' regimes far away from $\sigma/\sigma_{1,0} = 1$, where the analysis and experiments for square-base tanks established 'chaotic' regimes (there are no stable steady-state waves). For the cases in figures 13(d, e) the 'chaotic' waves are expected only in a narrow zone between U_2 and U_3, which will probably disappear owing to even damping.

4.3. *Effective frequency domains of stable steady-state motions versus base ratio*

The response curves of stable steady-state resonant waves show a considerable effect of a small disturbance $\mu = O(\epsilon^{2/3})$ of the base ratio $r = \mu + 1$ on the effective frequency domains of these waves, in general, and on the appearance of irregular 'chaotic' waves, in particular. Variation of the effective frequency domains versus r (in the $(\sigma/\sigma_{1,0}, r)$-plane) is exemplified in figures 14. Figure 14(a) shows four effective domains P_i, $i = 1, 2, 3, 4$ and an internal area corresponding to unstable 'planar' waves. It shows that, as was mentioned above, 'planar' motions remain unstable at $\sigma/\sigma_{1,0} = 1$ for r very close to 1 (for $0.97 < r < 1.09$ in our case), but become stable for larger deflections of the base ratio.

Further, figure 14(b) shows two effective areas of 'diagonal' waves: D_1 and D_2. The numerical analysis shows that the 'diagonal' resonant wave at $\sigma/\sigma_{1,0} = 1$ may only be realized for a small 'island' D_2. Moreover, if $r < 1$, the effective frequency domain (associated with D_1) shifts to the left of the primary resonance and the resonant 'diagonal' regime is not realized at all. In contrast, figure 14(c) predicts a predominating character of 'swirling' at $\sigma/\sigma_{1,0} = 1$ and $r \leqslant 1$ (in the area S_1) and, supplementary to that, a new zone of stable 'swirling' associated with S_2 appears.

In order to estimate the occurrence of 'chaotic' waves (no stable steady-state regimes) versus r and $\sigma/\sigma_{1,0}$, we overlapped the areas of instability from figures 14(a)–14(c) and marked the result in figure 14(d) by the shaded area. The figure shows that 'chaotic' waves appear for very small deflections of r around 1. However, because of the predominating character of the 'planar' (for increasing r) and 'swirling' (for decreasing r) regimes, the frequency domain of 'chaotic' waves becomes narrow for $r > 1.05$ and $r < 0.97$. This means that passage to a non-square base can lead to the disappearance of 'chaotic' motions.

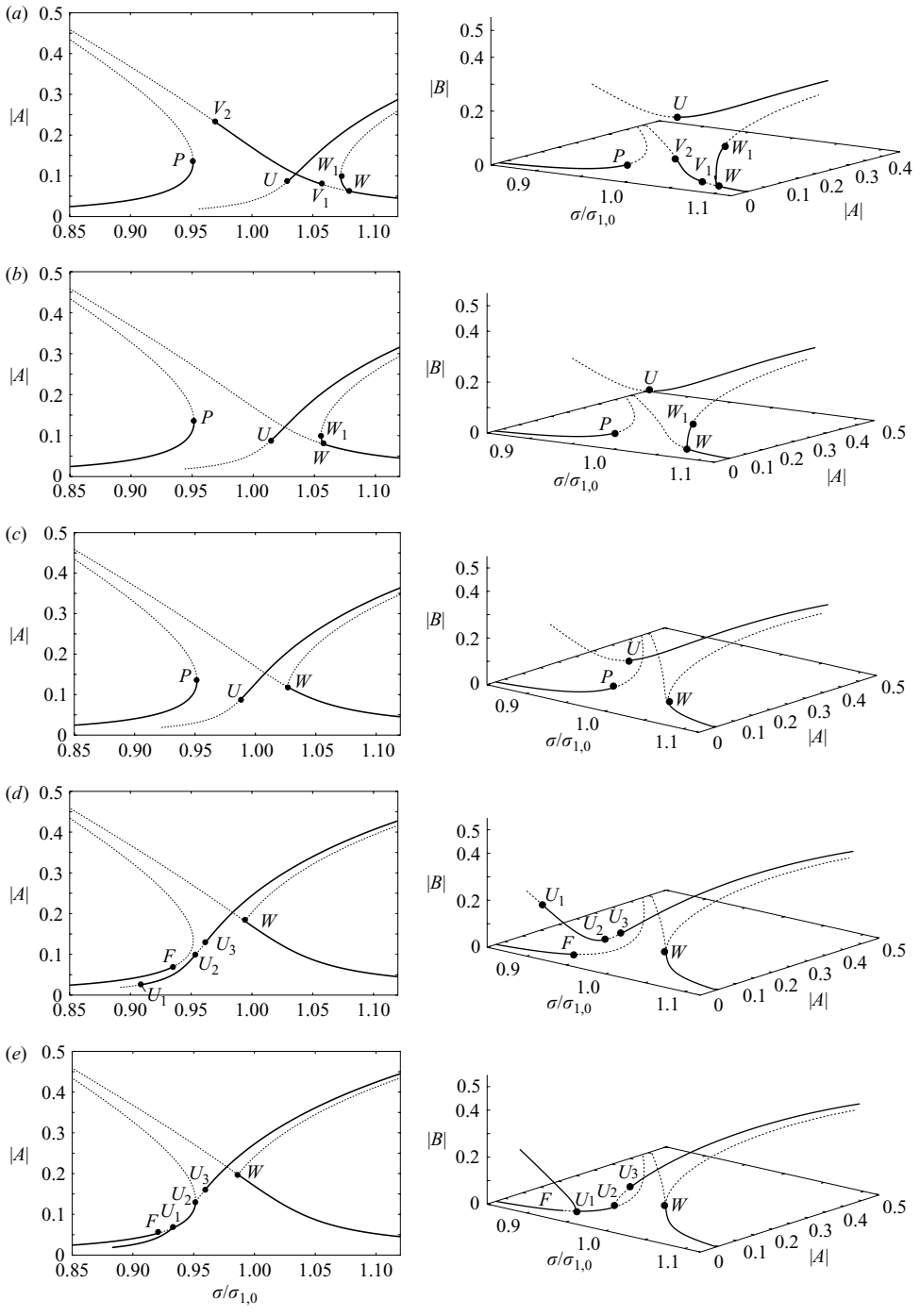

FIGURE 13. Resonance curves responsible for 'planar' and 'swirling' waves versus r for finite depths ($h > h_1$). The calculations are made for $h = 0.5$ and $\epsilon = 0.008$ related to our experiments. Four values of r are considered: (*a*) $r = 1.1$, (*b*) $r = 1.065$, (*c*) $r = 1$ (square cross-section), (*d*) $r = 0.9$ and $r = 0.87$. The graphs represent dependence of $|A|$ on $\sigma/\sigma_{1,0}$ and the three-dimensional branching in the $(\sigma/\sigma_{1,0}, |A|, |B|)$-coordinate system. Solid lines imply stable solutions and the dashed lines indicate instability of the corresponding branches. Point F is related to bifurcations leading to the 'diagonal' regime (see details in figure 12) and P is the turning point on the 'planar' curve response. The meaning of other points is explained in the main text.

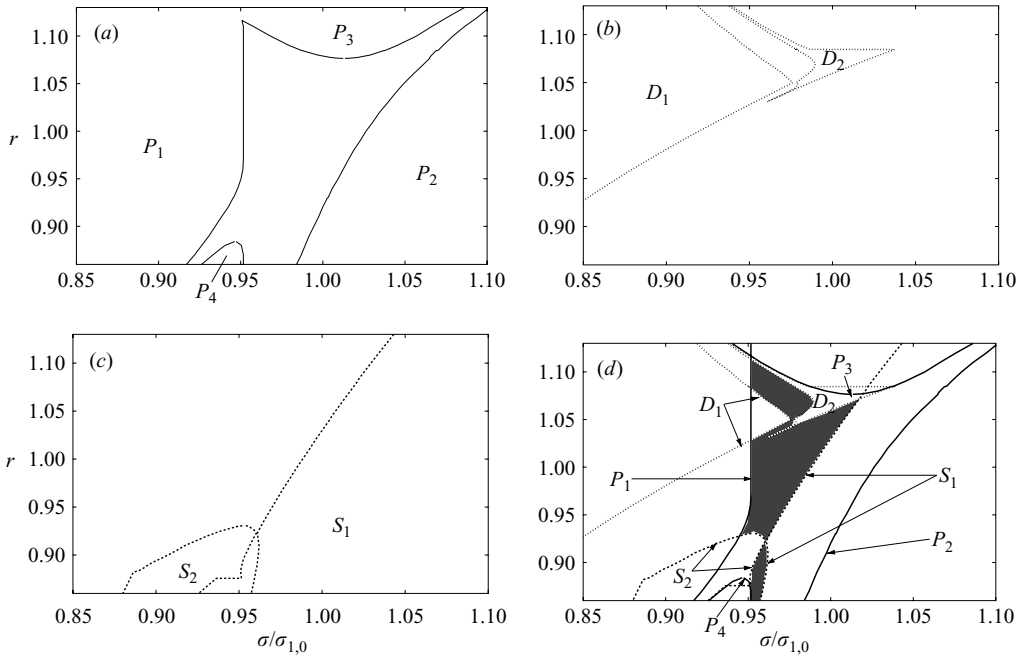

FIGURE 14. The domains of stability/instability of the steady-state motions in the $(\sigma/\sigma_{1,0}, r)$-plane for $h = 0.5$, $\epsilon = 0.008$. (*a*) shows the stability areas of 'planar' waves (P_i, $i = 1, 4$), (*b*) indicates the stability areas for 'diagonal' waves (D_1 and D_2) and (*c*) represents the stability domain S of 'swirling' waves. In order to detect the 'chaotic' wave motions (there are no stable steady-state regimes), the domains are superposed in (*d*). Evaluating the shaded area, which denotes 'chaotic', detects its narrowing for $r > 1.05$ and $r < 0.97$.

The classification of frequency domains becomes more complicated for $h < h_1$; we also found a larger area of 'chaotic' waves with increasing ϵ. However, as mentioned in Parts 1 and 2, both smaller depths and larger forcing amplitudes require modification of the Moiseyev asymptotic ordering, which is the theoretical background of the present paper.

The experimental tests on resonant sloshing in tanks with a nearly square base have been performed with the same experimental set-up as in Part 2, but for a base $60 \times 66\,\mathrm{cm}^2$. Two forcing amplitudes 0.048 m and 0.096 m were tested corresponding to $\epsilon = 0.008$ and 0.016, respectively. Similarly, as described in previous publications, pure periodic waves in nearly square geometry were not detected even after 270–350 forcing periods for most of the test cases with three-dimensional waves, because of local breaking phenomena and consequent amplification of steep waves. However, these relatively steep waves did not affect the global smooth flows and the visual observations clearly identified 'planar' and 'swirling' as well as waves of irregular 'chaotic' character. We present theoretical estimates of the types of motion and corresponding experimental observations in figure 15 for $r = 60/66$ (excitations along the longer walls were unfortunately not tested in experiments). Figure 15(*a*) presents results for smaller forcing amplitude and figure 15(*b*) gives results for larger amplitude. These results are in good agreement.

The first conclusion from comparisons in figure 15(*a*) is that $r = 60/66$ reduces the actual zone of 'chaotic' waves. The theory in figure 15(*a*) finds it only between u_2 and u_3 and this is too narrow to be captured in experiments. For the analogous forcing

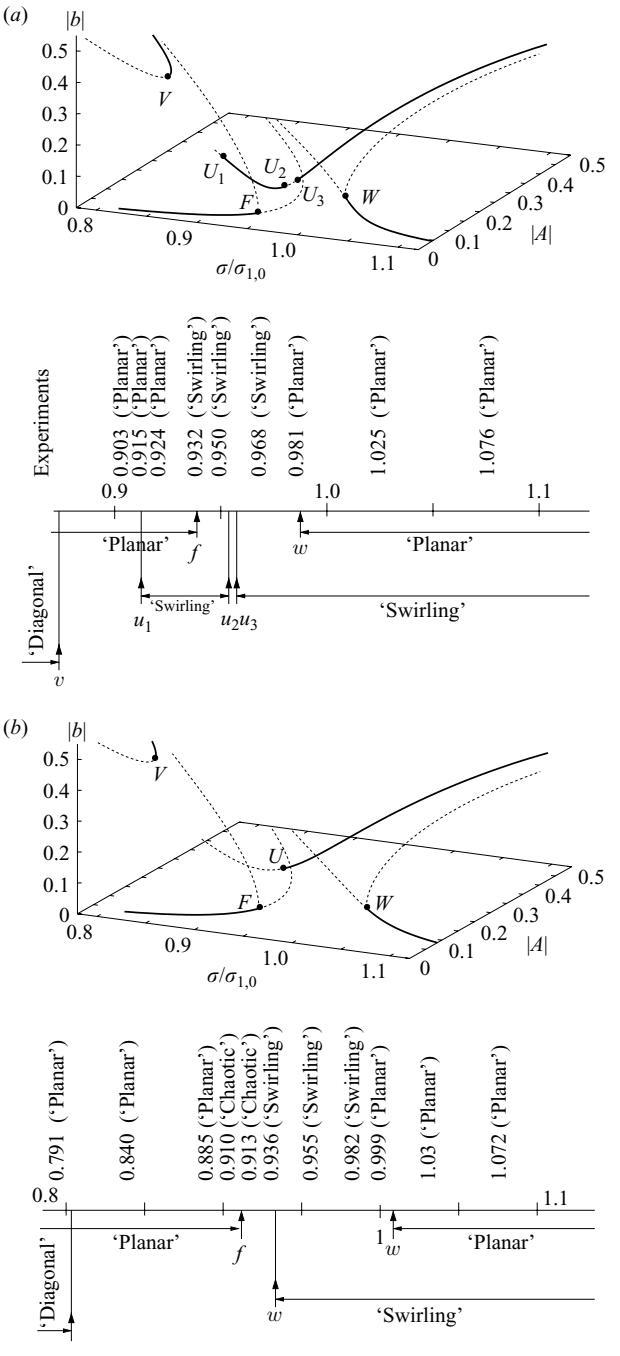

FIGURE 15. Response curves implying the steady-state resonant sloshing in a near-square tank with $r = 60/66$. The graphs are given in the $(\sigma/\sigma_{1,0}, |A|, |b|)$-coordinate system ($b = \sqrt{B^2 + \bar{B}^2}$), the three-dimensional curves represent three-dimensional wave motions, but two-dimensional branches in the $(\sigma/\sigma_{1,0}, |A|)$-plane determine the 'planar' regime. Points on the solid lines correspond to stable solutions and the dashed curves denote instability. The meaning of the bifurcation points P, F, W etc. is explained in figures 12 and 13. The abscissa of these points (p, f, w etc.) intersect the ranges where different steady-state waves are stable. Resulting stability frequency domains are drawn for each case: (*a*) $\epsilon = 0.008$ and (*b*) $\epsilon = 0.016$.

amplitude of the $60 \times 60\,\mathrm{cm}^2$ square tank, Part 1 detected a significant domain of 'chaotic' motions. Larger excitation amplitude obviously increases the 'chaotic' waves zone (now it is situated between f and w). Two experimental runs confirmed its existence. However, this domain is still small relative to analogous forcing of the $60 \times 60\,\mathrm{cm}^2$ square tank in Part 1.

The most evident fact, which has been confirmed experimentally, is the presence of the stable 'planar' waves at the primary resonance $\sigma/\sigma_{1,0} = 1$. We concluded in Part 1 that the local vicinity of the primary resonance always implies three-dimensional wave regimes for square-base basins, at least, for the finite fluid depth. Examples in figure 15 demonstrate the opposite case for near-square tanks. There is also experimental confirmation of the theoretical prediction that the 'swirling' regime for $r < 1$ can be expected far away from the primary resonance. The experimental observations of the 'swirling' waves at $\sigma/\sigma_{1,0} = 0.932$ (case a) and $\sigma/\sigma_{1,0} = 0.936$ (case b) correspond to the frequency domain where excitations of the square-base tanks resulted in 'planar' waves (see, almost similar results in figures 5 (d) and 11 of Part 1).

The agreement between theoretical predictions and experimental data is especially good for the smaller $\epsilon = 0.008$, but a discrepancy between the theory and experiments for larger amplitude (see points at $\sigma/\sigma_{1,0} = 0.999$ and 0.910) is quantified to be in the order of ϵ. Because our asymptotic scheme guarantees the results for $\sigma/\sigma_{1,0}$ in the order of $O(\epsilon^{2/3})$, this small discrepancy does not indicate a failure of the asymptotic theory.

5. Concluding remarks and discussion

The main results of the present paper consist of generalizing those from Part 1 for relevant prismatic tanks with an almost square base. Two experimental series with the 60×66 cm^2 base tank, which are analysed in § 4.3, have been conducted within the framework of preparation of Part 2, in parallel with analogous experiments with the square 60×60 cm^2 base tank. The emphasis was on types of steady-state regimes with the same forcing amplitudes and on effective frequency domains of these regimes. The result was that, on the one hand, both geometries exhibit the same type of steady-state wave regime, but, on the other hand, the effective frequency domains of these regimes differ considerably. In one experimental series with the 60×66 cm^2 base tank, we were not even able to find 'chaotic' waves, but analogous excitations of the square-base tank clearly exhibited a sufficient frequency range where irregular, 'chaotic' motions occur. Hence, the relevance of non-square-base tanks and the striking experimental observations have formed the objective of the present investigations: to describe steady-state wave regimes and quantify their effective frequency domains versus the base ratio r. We restricted ourself to finite fluid depths, i.e. the depth/breadth ratio is larger than $h_1 = 0.3368\ldots$ (h_1 is the critical depth computed by Waterhouse 1994; Faltinsen *et al.* 2003), and, under certain asymptotic assumptions matching the scaled forcing amplitude ϵ with deviations of the base ratio $\mu = r - 1 = O(\epsilon^{2/3})$, performed mathematically tedious analysis of local branching of the response curves implying the dominating steady-state wave amplitudes. The results are documented in § 4. These confirmed the existence of the same steady-state waves as in tanks of square base and demonstrated that small non-zero μ may redistribute effective frequency domains significantly. Good agreement with two experimental series was established.

Later on, we found a mismatch between our theoretical and experimental results and applied mathematical results by Bridges (1985, 1987) who studied free-standing

in tanks of nearly square base and did not report 'swirling'. In order to clarify whether 'swirling' appears only for resonant waves, we conducted an independent asymptotic analysis based on the modal technique. Our derivations showed the presence of free-standing 'swirling' formed by the lowest (1, 0)–(0, 1)-dominating modes, for the case, which has not been analysed by Bridges (1985, 1987). The details are given in § 3.

In contrast to Part 2, the present paper did not pursue simulations of resonant waves, any estimates of damping and/or consequent experimental validation of steady-state and transient amplitudes. The present modal system captures only the smooth dominating component of the resonant flows and, obviously, it is of limited applicability for quantitative validation of, for instance, wave elevations. However, we believe that successful simulations are possible (limited by occurrence of local phenomena) by using the appropriate adaptive multimodal models developed in Part 2. The present studies can also be generalized to more complicated excitation, e.g. motion along the diagonal of the rectangular base as well as angular motions. Further, the theoretical results by Ockendon *et al.* (1996) and Ockendon & Ockendon (2001) on imperfections of the wall for the shallow-fluid sloshing suggest future investigations for resonant regimes in nearly square tanks with non-flat walls, for intermediate depths and so on. This should require significant modifications of the modal technique (see Faltinsen & Timokha 2002). A special problem consists of the theoretical description of the local phenomena that have been found in our experiments and reported by many others (Faltinsen *et al.* 2003; Royon, Hopfinger & Cartellier 2005).

REFERENCES

Bridges, T. J. 1985 On secondary bifurcation of three dimensional standing waves. Technical Summary Report Wisconsin Univ., Madison.

Bridges, T. J. 1986 On secondary bifurcation of three-dimensional standing waves. *SIAM J. Appl. Maths* **47**, 40–59.

Bridges, T. J. 1987 Secondary bifurcation and change of type for three dimensional standing waves in finite depth. *J. Fluid Mech.* **179**, 137–153.

Bryant, P. J. & Stiassnie, M. 1994 Different forms for nonlinear standing waves in deep water. *J. Fluid Mech.* **272**, 135–156.

Bryant, P. J. & Stiassnie, M. 1995 Water waves in a deep square basin. *J. Fluid Mech.* **302**, 65–90.

Faltinsen, O. M. 1974 A nonlinear theory of sloshing in rectangular tanks. *J. Ship Res.* **18**, 224–241.

Faltinsen, O. M., Rognebakke, O. F., Lukovsky, I. A. & Timokha, A. N. 2000 Multidimensional modal analysis of nonlinear sloshing in a rectangular tank with finite water depth. *J. Fluid Mech.* **407**, 201–234.

Faltinsen, O. M., Rognebakke, O. F. & Timokha, A. N. 2003 Resonant three-dimensional nonlinear sloshing in a square base basin. *J. Fluid Mech.* **487**, 1–42.

Faltinsen, O. M., Rognebakke, O. F. & Timokha, A. N. 2005*a* Resonant three-dimensional nonlinear sloshing in a square base basin. Part 2. Effect of higher modes. *J. Fluid Mech.* **523**, 199–218.

Faltinsen, O. M., Rognebakke, O. F. & Timokha, A. N. 2005*b* Classification of three-dimensional nonlinear sloshing in a square-base tank with finite depth. *J. Fluids Struct.* **20**, 81–103.

Faltinsen, O. M. & Timokha, A. N. 2002 Asymptotic modal approximation of nonlinear resonant sloshing in a rectangular tank with small fluid depth. *J. Fluid Mech.* **470**, 319–357.

Feng, Z. C. & Sethna, P. R. 1989 Symmetry-breaking bifurcations in resonant surface waves. *J. Fluid Mech.* **199**, 495–518.

Keulegan, G. H. 1959. Energy dissipation in standing waves in rectangular basin. *J. Fluid Mech.* **6**, 33–50.

Kopachevsky, N. D. & Krein, S. G. 2003 Operator approach to linear problems of hydrodynamics. Vol. 2. Nonself-adjoint problems for viscous fluids. Operator Theory: Advances and Applications, 146. Birkhuser, Basel.

Krein, S. G. 1964 Oscillations of a viscous fluid in a container. *Dokl. Akad. Nauk. SSSR* **159**, N 2, 262–265 (in Russian).

Krein, S. G. & Langer, H. 1978*a* On some mathematical principles in the linear theory of damped oscillations of continua. *Integral Equations Operator Theory*, N 3, pp. 364–399.

Krein, S. G. & Langer, H. 1978*b* On some mathematical principles in the linear theory of damped oscillations of continua. II. *Integral Equations Operator Theory*, N 3, pp. 539–566.

Martel, C., Nicolas, J. A. & Vega, J. M. 1998 Surface-wave damping in a brimful circular cylinder. *J. Fluid Mech.* **360**, 213–228.

Miles, J. W. 1984 Resonantly forces surface waves in circular cylinder. *J. Fluid Mech.* **149**, 15–31.

Miles, J. W. 1994 Faraday waves: rolls versus squares. *J. Fluid Mech.* **269**, 353–371.

Miles, J. W. & Henderson, D. M. 1998 A note on interior *vs.* boundary layer damping of surface waves in a circular cylinder. *J. Fluid Mech.* **364**, 319–323.

Moiseyev, N. N. 1958 To the theory of nonlinear oscillations of a limited liquid volume of a liquid. *J. Appl. Math. Mech. (PMM)* **22**, 612–621 (in Russian).

Narimanov, G. S. 1957 Movement of a tank partly filled by a fluid: the taking into account of non-smallness of amplitude. *J. Appl. Maths Mech. (PMM)* **21**, 513–524 (in Russian).

Ockendon, H. & Ockendon, J. R. 2001 Nonlinearity in fluid resonances. *Meccanica* **36**, 297–321.

Ockendon, H., Ockendon, J. R. & Waterhouse, D. D. 1996 Multi-mode resonance in fluids. *J. Fluid Mech.* **315**, 317–344.

Royon, A., Hopfinger, E. J. & Cartellier, A. 2005 Nonlinear wave motions in containers and wave breaking characteristics. *Hydrodynamics VI – Theory and Applications* (ed. L. Cheng & K. Yeow), pp. 555–561.

Waterhouse, D. D. 1994 Resonant sloshing near a critical depth. *J. Fluid Mech.* **281**, 313–318.